PHYSICAL REVIEW FLUIDS **2**, 093701 (2017)

Growth and detachment of single hydrogen bubbles in a magnetohydrodynamic shear flow

Dominik Baczyzmalski*
Institute of Fluid Mechanics and Aerodynamics, Universität der Bundeswehr München, D-85577 Neubiberg, Germany

Franziska Karnbach
IFW Dresden, Institute for Complex Materials, D-01069 Dresden, Germany and Faculty of Mechanical Science and Engineering, Technische Universität Dresden, D-01062 Dresden, Germany

Gerd Mutschke, Xuegeng Yang, and Kerstin Eckert
Helmholtz-Zentrum Dresden–Rossendorf, Institute of Fluid Dynamics, D-01314 Dresden, Germany

Margitta Uhlemann
IFW Dresden, Institute for Complex Materials, D-01069 Dresden, Germany

Christian Cierpka
Institute of Thermodynamics and Fluid Mechanics, Technische Universität Ilmenau, D-98684 Ilmenau, Germany
(Received 23 June 2017; published 15 September 2017)

This study investigates the effect of a magnetohydrodynamic (MHD) shear flow on the growth and detachment of single sub-millimeter-sized hydrogen gas bubbles. These bubbles were electrolytically generated at a horizontal Pt microelectrode (100 μm in diameter) in an acidic environment (1 M H_2SO_4). The inherent electric field was superimposed by a homogeneous electrode-parallel magnetic field of up to 700 mT to generate Lorentz forces in the electrolyte, which drive the MHD flow. The growth and motion of the hydrogen bubble was analyzed by microscopic high-speed imaging and measurements of the electric current, while particle tracking velocimetry (μPTV) and particle image velocimetry (μPIV) were applied to measure the surrounding electrolyte flow. In addition, numerical flow simulations were performed based on the experimental conditions. The results show a significant reduction of the bubble growth time and detachment diameter with increasing magnetic induction, which is known to improve the efficiency of water electrolysis. In order to gain further insight into the bubble detachment mechanism, an analysis of the forces acting on the bubble was performed. The strong MHD-induced drag force causes the bubble to slowly slide away from the center of the microelectrode before its detachment. This motion increases the active electrode area and enhances the bubble growth rate. The results further indicate that at large current densities the coalescence of tiny bubbles formed at the foot of the main bubble might play an important role for the bubble detachment. Moreover, the occurrence of Marangoni stresses at the gas-liquid interface is discussed.

DOI: 10.1103/PhysRevFluids.2.093701

I. INTRODUCTION

The development of efficient energy storage systems has become a field of great relevance in view of the growing worldwide application of renewable energies. In particular, high expectations

*dominik.baczyzmalski@unibw.de

are now placed on chemical energy storage in the form of hydrogen because of its high energy density and the possibility to generate it directly from the electricity produced by renewable energy sources via water electrolysis. However, the relatively low efficiency of this process has been a major drawback for its establishment on an industrial scale in the past. A significant part of the losses is associated with the formation of hydrogen and oxygen gas bubbles, which reduce the active area on the electrode as well as the effective conductivity of the electrolyte [1–4]. Therefore, the accelerated removal of these gas bubbles from the electrode surface and the bulk electrolyte is essential to improve the performance of the process and allow for its operation at higher currents, hence higher production rates [5,6]. Forced convection has long been recognized as an effective method to reduce the void fraction in the interelectrode gap by a faster bubble transport [7–9]. More important, it enhances the bubble detachment from the electrode, thereby reducing the fraction of the electrode covered by bubbles [10–12]. In this context, the application of magnetic fields has recently attracted much interest [13–18]. Since the electric current density $\mathbf{j}$ is already present during the electrolytic process, the superposition of a magnetic field $\mathbf{B}$ gives rise to a Lorentz force density $\mathbf{f_L} = \mathbf{j} \times \mathbf{B}$, which acts as a body force directly on the electrolyte surrounding the growing bubble and causes the so-called magnetohydrodynamic (MHD) flow.

In general, two different magnetic field orientations, electrode-normal and electrode-parallel fields, have been investigated in the past. Koza *et al.* [14] showed that both configurations are able to reduce the bubble detachment size and bubble coverage on the electrode. In the case of an electrode-normal magnetic field, the generated MHD flow acts in the azimuthal direction with different signs on the upper and lower parts of the bubble. It was hypothesized that this flow forms a region of lower pressure above the bubble and thereby facilitates the detachment of the bubble. However, recent experimental and numerical studies [19,20] indicate that the pressure change is too low to cause such a considerable lift force. Another possible explanation for the enhanced bubble detachment is the additive effect of a group of bubbles, causing a strong global shear flow along the electrode as indicated by the experiments presented in Ref. [19].

A wall-parallel shear flow is also directly generated when the magnetic field is oriented parallel to the electrode [21,22]. The forces acting on a bubble in the presence of a shear flow were widely investigated for vapor bubbles in forced convection boiling (see, e.g., Refs. [23–27]) as well as for bubbles formed at orifices [28]. The hydrodynamic forces imposed by the shear flow, i.e., the drag and lift forces, usually help to reduce the bubble detachment size. In forced convection boiling, bubble departure from the nucleation site and sliding along the heater surface is often observed prior to detachment [23]. Force balance analyses were also performed for gas-evolving electrodes to predict the bubble detachment size and the bubble coverage of the electrode [11,12]. However, despite extensive research efforts, important aspects of the growth and detachment dynamics of electrolytic gas bubbles are not fully understood yet. This includes, for instance, coalescence phenomena [29,30], wettability [31] and electrowetting effects [32], and the influence of dissolved hydrogen and its concentration gradients on the surface tension, which give rise to Marangoni stresses at the gas-liquid interface [33,34]. Furthermore, the hydrodynamic force acting on a bubble in a shear flow cannot be directly transferred to the case of a MHD shear flow, since the underlying flow effects highly depend on the local Lorentz force distribution around the bubble. Therefore, a detailed investigation of the growth and detachment of electrolytic gas bubbles in a MHD shear flow is necessary to gain further insight.

At practical current densities, the bubble coverage and void fraction near the electrode is very high, making it almost impossible to analyze the bubble growth dynamic or measure the electrolyte flow [22,35]. Moreover, the layer of detached bubbles rising near the electrode can generate a strong electrolyte convection with high velocity fluctuations caused by bubble-induced pseudoturbulence as well as shear-induced turbulence [22]. This further complicates the analysis as the effect of the bubble-induced flow and the MHD flow cannot be easily separated. For the above-mentioned reasons, nano- or microelectrodes were employed in many studies to generate single hydrogen

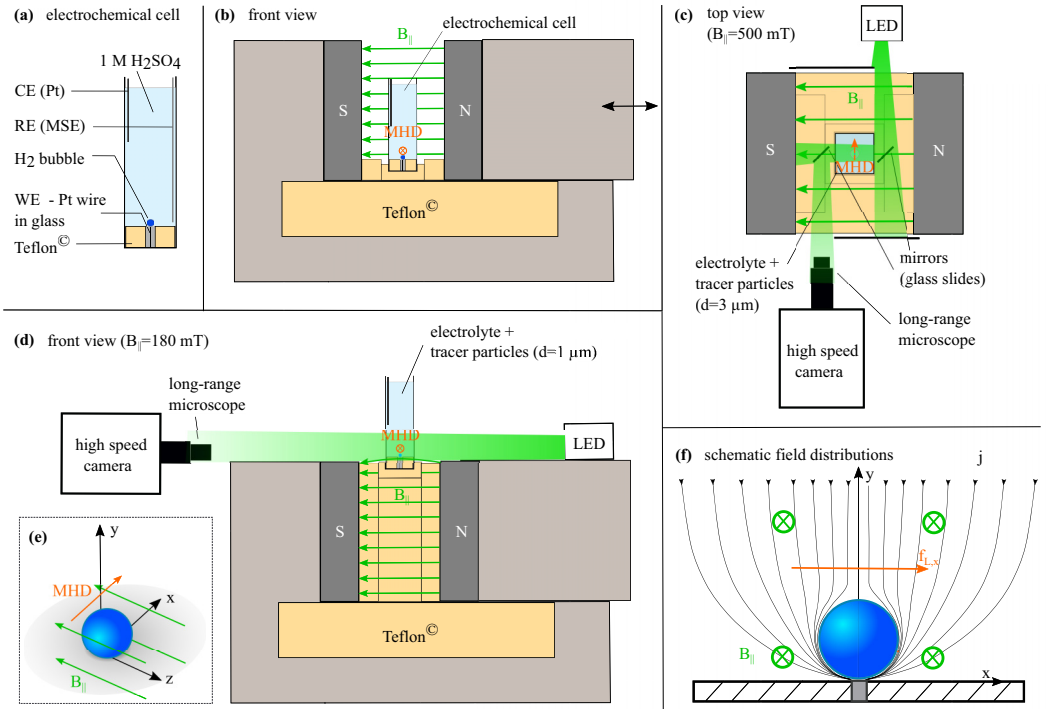

FIG. 1. Setup: The electrochemical cell (a) was placed in an electrode-parallel homogeneous magnetic field generated by two magnets (b). The spacing between the two magnets was adjustable so that the magnetic induction $B_{||}$ could be varied between 500 and 700 mT. [(c), (d)] Long-range microscopy paired with shadowgraphy served to measure the bubble dynamics and the 2D velocity field around the bubble via PTV/PIV. (c) For $B_{||} = 500$ mT, the backlight was guided by mirrors to image the main flow plane. (d) For $B_{||} = 180$ mT, the cell had to be placed above the two magnets to enable the low magnetic induction. (e) The coordinate system lies in the center of the electrode. (f) Schematic illustration of the current distribution $\mathbf{j}$ in the case of a hydrogen bubble evolving at the center of the electrode ($x = 0$). The Lorentz forces $\mathbf{f_L} = \mathbf{j} \times \mathbf{B}$ act mainly in the x direction.

bubbles at a known position [20,29–31,36–41]. The current distribution in this case is somewhat different compared to larger electrodes as the entire current has to pass through the smaller electrode area. This causes a strong increase of the current density close to the foot of the bubble, as can be seen in Fig. 1(f). Nonetheless, this approach allows for thorough investigations of the bubble growth dynamics and electrolyte convection. In this study, a horizontal Pt microelectrode (100 μm in diameter) was used to analyze the growth and detachment dynamics of hydrogen bubbles evolving in a MHD shear flow. For the first time, detailed measurements of the surrounding MHD flow are provided. The experimental results are supported by additional numerical simulations, which enables us to estimate the magnitude of the hydrodynamic forces acting on the bubble and assess their role in the bubble detachment.

The structure of the paper is as follows. First, the electrochemical setup, the applied measurement techniques, and the numerical methods are described in detail. The bubble growth dynamics are analyzed in the next section, followed by the results of the MHD flow measurements and the numerical simulations. Using the experimental and the numerical data, the forces acting on a bubble are then discussed. The results are finally summarized in the last section.

II. EXPERIMENTAL AND NUMERICAL METHODS

A. Electrochemical setup

A specialized electrochemical setup, described in detail in Ref. [36], was used to generate single hydrogen bubbles at a horizontal microelectrode. The setup comprises a cuboid glass cuvette (Hellma, $45 \times 10 \times 10$ mm^3 [H $\times$ W $\times$ D]) as the electrochemical cell and three electrodes. A Pt wire ($d = 1$ mm, 99.99% purity) was used as the counterelectrode (CE), while a mercury/mercurous sulfate electrode [MSE; 650 mV vs standard hydrogen electrode (SHE)], connected through a salt bridge filled with electrolyte, served as the reference electrode (RE). All potentials mentioned in the following are referred to MSE. Both the counterelectrode and reference electrode were placed into the cell from the top [see Fig. 1(a)]. A Pt microelectrode ($d = 100$ μm, 99.99% purity), fused into a glass capillary with a diameter of 6 mm, was used as the working electrode (WE). The WE was inserted into a Teflon plate which formed the bottom of the cell and is electrically connected via a copper block. It should be noted that the quality of the electrode surface preparation plays an important role in the reproducibility of the experiment. A special surface polishing procedure as described by Karnbach *et al.* [36] was therefore applied. All electrodes were connected to a potentiostat (Zahner Zennium electrochemical workstation), which was used to conduct the experiments under potentiostatic conditions (constant voltage between WE and RE) and measure the electric current transient during the periodic bubble growth cycle. As electrolyte, a 1 M H_2SO_4 (aqueous) solution was used to generate single hydrogen bubbles as shown in previous works [20,29,36]. All measurements were carried out at room temperature.

An in-house-designed (IFW Dresden) magnet was used to superimpose a homogeneous electrode-parallel magnetic field [see Fig. 1(b)]. It consists of two NdFeB permanent magnets ($40 \times 40 \times 20$ mm^3 [H $\times$ W $\times$ D]) which are connected through an iron yoke, made of ARMCO iron. This allows for a uniform and homogeneous magnetic field over the whole electrochemical cell, which was centrally placed between the magnets onto a Teflon block that was integrated into the inside of the iron yoke. The distance between the magnets was adjustable, which allowed for the variation of the magnetic induction $B_{||}$ between 500 and 700 mT. Additional investigations were performed in a weaker magnetic field by placing the cell slightly above the magnets [see Fig. 1(d)]. There, the measured magnetic induction at the position of the electrode was approximately $B_{||} = 180$ mT and decreased with the electrode-normal distance. However, high values of the Lorentz force $\mathbf{f_L} = \mathbf{j} \times \mathbf{B}$ are only generated close to the bubble due to the high local current density $\mathbf{j}$ [see Fig. 1(f)]. In this region, the magnetic field can be considered to be homogeneous. It should be also mentioned that although the orientation of the CE is vertical (as opposed to the horizontal WE), it has virtually no effect on the resulting Lorentz force distribution. Since the CE was positioned far away from the WE and its surface is much larger, the current density and thus the corresponding Lorentz forces are negligible in this region.

As a reference, another set of electrochemical measurements was performed in the absence of the magnetic field ($B_{||} = 0$ mT). Most experiments were carried out at a constant potential of $E = -2.0$ V and focused on the effect of the magnetic field. A few additional experiments were performed at a lower potential of $E = -1.5$ V to examine the influence of the electrode potential.

B. Measurements of the bubble dynamics and MHD flow

As sketched in Fig. 1(f), the Lorentz forces generated by the magnetic field ($\mathbf{f_L} = \mathbf{j} \times \mathbf{B}$) act in the plane perpendicular to the magnetic field. Thus, both the bubble dynamics and the flow field in this plane (xy plane) are of particular interest. Since a direct optical access to that plane is not possible due to the magnets, a mirror setup was employed as illustrated in Fig. 1(c). This was only applicable for $B_{||} = 500$ mT since the spacing between the magnets had to be large enough to place the mirrors. To exclude possible magnetic field distortions by the magnetic coatings of typical mirrors, two 1-mm-thick glass slides cut into 4-mm-wide pieces were used as mirrors. Polystyrene tracer particles with a diameter of 3 μm were added to the solution to measure the

electrolyte flow. Both the particles and the growing bubble were simultaneously visualized by means of shadowgraphy. The background illumination was provided by a multichannel light-emitting diode (LED) operating in a wide wavelength range (Lumencor SPECTRA X light engine). The shadowgraph images were recorded by a high-speed camera (PCO DIMAX by PCO GmbH) equipped with a long-range microscope objective at a frame rate of 500 fps. This allowed for detailed measurements with a magnification of about $M = 8.3$ and a resolution of $0.75\,\text{pixel}/\mu\text{m}$. The bubble geometry and position was extracted from the shadow images by several image-processing steps, including background removal, segmentation of the bubble image, and applying a circular fit to the identified bubble contour. The two-dimensional (2D) velocity field around the bubble was obtained using time-resolved particle tracking velocimetry (PTV). Since the light reflection by the glass slide is weak and the reflection from its rear side is causing additional undesired shadows, a relatively low tracer particle concentration was used to obtain a sufficient signal-to-noise ratio and ensure a reliable identification of individual particle images. The effective depth of focus (i.e., the measurement depth) was reduced by a proper image preprocessing [42,43] and was experimentally estimated to be less than 100 μm. This is sufficiently small in view of the observed bubble sizes of up to 500 μm. Moreover, the obtained velocity data was phase averaged to allow for a much higher measurement resolution and better statistics, despite the low particle concentration. This is possible since the bubble evolution cycle is very periodic, as will be demonstrated later. Therefore, several hundred periodic bubble cycles were recorded, the data of which were divided into 20 equally spaced phase intervals. The required phase information can be easily obtained from the simultaneously measured current signal [20,29]. The resulting phase-resolved data was binned onto a grid of 20×20 pixels ($26.4 \times 26.4\ \mu\text{m}^2$).

For the second set of measurements at $B_{||} = 180$ mT, the optical access from the side was possible without the use of mirrors [see Fig. 1(d)], which significantly increased the contrast of the shadow images. The experimental arrangement required a larger working distance, leading to a higher field of view with a slightly lower magnification of about $M = 6.9$ and a resolution of $0.63\,\text{pixels}/\mu\text{m}$. Moreover, the improved image contrast allowed for a significantly higher particle concentration and the use of smaller particles (1 μm), which defocus earlier and thereby increase the measurement resolution in depth direction. The 2D velocity field was obtained by particle image velocimetry (PIV) using a final interrogation window size of 24×24 pixels ($38 \times 38\ \mu\text{m}^2$) with an overlap of 50%. This method is far less time-consuming at high particle concentrations than PTV. However, PTV was additionally applied in a smaller region around the bubble to better resolve the high velocity gradients [44] that have been observed close to the gas-liquid interface. A bin size of 10×10 pixels ($16 \times 16\ \mu\text{m}^2$) was used for the PTV data. Both the PIV and PTV data were then phase averaged (40 phase intervals) and merged together.

It should be mentioned that additional investigations were performed to verify that the cell walls do not influence the resulting flow significantly. Therefore, the three-dimensional bulk flow was measured using astigmatism tracking velocimetry (APTV [45]), a single-camera three-dimensional volumetric particle-tracking technique (for more details on the setup, see Ref. [20]). It was found that, for all investigated cases, the cell dimensions are sufficiently large and have virtually no influence on the near-bubble flow. This is due to the fact that high values of the current density and the Lorentz forces only occur in close proximity to the microelectrode and the evolving bubble.

C. Numerical model

Finite element simulations were performed to gain further insight and to analyze the hydrodynamic forces that are imposed on the bubble. As inertial effects of the flow and the Lorentz force can be neglected in a first approximation, steady simulations were carried out. These simulations closely match the experimental conditions at $B_{||} = 500$ mT and $E = -2.0$ V for a late phase of the bubble growth, representing the situation close to bubble detachment. A spherical bubble model with a diameter of 408 μm and centroid position of $x_c = 80$ μm and $y_c = 210$ μm was used according to the observations shown in Fig. 4 at approximately 115 ms after the formation of the bubble. The outer

geometry of the three-dimensional domain was set according to the aforementioned cell dimensions. Assuming a nonconductive gaseous phase (bubble) and a constant electrical conductivity σ_e of the 1 M H_2SO_4 electrolyte, the primary electric current density $\mathbf{j}$ was obtained by solving the Laplace equation for the electric potential Φ

$$\Delta\Phi = 0, \quad \mathbf{j} = \sigma_e \nabla\Phi. \tag{1}$$

The boundary conditions at the microelectrode and the counterelectrode were set such as to match the electric current observed in the experiment. The current density is very low at the counterelectrode, since its size is much larger than the microelectrode and the distance between those electrodes is large. Therefore, the entire upper wall of the cell was modeled as the counterelectrode for simplicity. At the remaining walls and at the bubble surface, no-flux conditions $\partial j/\partial n = 0$ were applied (n denotes the respective normal direction). Although not taken into account in the following, we would like to mention that the distribution of hydrogen dissolved in the electrolyte can be computed by solving a convection-diffusion equation whereby the rate of hydrogen production at the electrode follows from Faraday's law [20,46]. The electrolyte flow was simulated using the incompressible Navier-Stokes equations including the Lorentz force $\mathbf{f_L} = \mathbf{j} \times \mathbf{B}$.

$$\rho_0 \, (\mathbf{u}\nabla)\, \mathbf{u} = -\nabla p + \mu \, \Delta\mathbf{u} + \mathbf{f_L}, \quad \nabla \cdot \mathbf{u} = 0. \tag{2}$$

Here, ρ_0 and μ denote the density and the dynamic viscosity of the electrolyte, respectively. The buoyancy force accounting for density gradients due to changes of the electrolyte composition can be neglected compared to the Lorentz force. A no-slip condition $\mathbf{u} = 0$ was applied at all boundaries except for the gas-liquid interface, where a free slip condition was used as the bubble is considered to be free of immobilizing surfactants. The boundary conditions for a stationary bubble (with negligible viscosity and density compared to the liquid phase) were set accordingly to

$$\mathbf{u} \cdot \mathbf{n} = 0, \quad [-p\hat{\mathbf{I}} + \mu(\nabla\mathbf{u} + (\nabla\mathbf{u})^T)]\mathbf{n} = 0, \tag{3}$$

where $\hat{\mathbf{I}}$ and $\mathbf{n}$ denote the identity tensor and the normal unit vector, respectively. The simulations were performed using COMSOL V.5.3 with an unstructured grid of approximately 650 000 triangular elements, which was properly refined in the vicinity of the electrode and the bubble.

III. RESULTS AND DISCUSSION

A. Bubble dynamics

The electrochemical reactions that take place during the electrolysis of water generate hydrogen gas at the microelectrode (cathode). The amount of the generated hydrogen gas is related to the electric current I that passes through the electrode by Faraday's law [29]

$$n_{H_2} = \frac{\int I(t)dt}{zF} \tag{4}$$

where n_{H_2}, z, and F denote the number of moles of the generated hydrogen, the charge number, and the Faraday constant, respectively. As the electrolyte adjacent to the electrode becomes highly supersaturated with dissolved hydrogen (up to several orders of magnitude greater than the saturation value [1,47]), gas bubbles will nucleate and grow in size until they are able to detach from the nucleation site. The bubble formation on a microelectrode in an acidic environment is a highly periodic cycle [29,30]. This growth cycle is characterized by oscillations of the current as illustrated in Fig. 2(a). Each bubble growth cycle begins and ends shortly before the peak value of the absolute current is reached. The detachment of the bubble is almost immediately followed by the nucleation of the next bubble on the electrode; i.e., the waiting time necessary for the nucleation of a bubble is very small [29]. The change of the current during the bubble growth is associated with a reduction of the active electrode area, which alters the current distribution and changes the resistance [30]. As expected, the magnitude of the current becomes larger when the absolute potential is increased from -1.5 to -2.0 V [see Fig. 2(a)]. Moreover, the absolute current generally increases with the

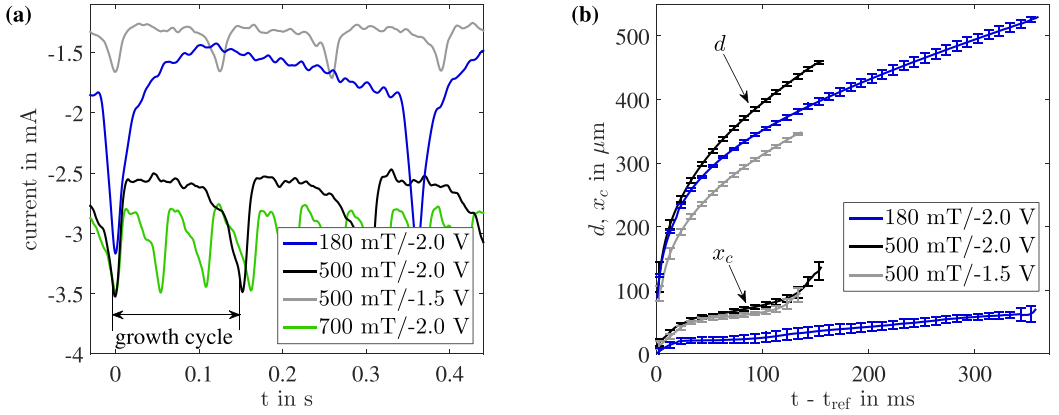

FIG. 2. (a) Current oscillations associated with the periodic evolution of single hydrogen bubbles for different values of the magnetic induction and electrode potential. Each growth cycle begins and ends shortly before the peak value of the absolute current. (b) Corresponding evolution of the bubble diameter d and its wall-parallel centroid position x_c. The diameter follows approximately a $d \propto t^{1/3}$ relationship. Data of 100–900 bubbles were considered depending on the measured configuration. The error bars represent twice the standard deviation ($\pm 2\sigma$).

applied magnetic induction, which can be attributed to the MHD-induced drag force that moves the growing bubble away from the microelectrode [Fig. 2(b)] and increases its active area. This will be demonstrated later in more detail. Another effect that may also contribute to the increase of the absolute current with the magnetic induction is the enhanced ion transport induced by the MHD convection.

Figure 2(b) shows the periodic evolution of the bubble diameter based on the image evaluation of several hundred growth cycles. An increase of the current magnitude, caused by applying either a higher absolute electrode potential or magnetic induction, enhances the growth rate of the bubble since more hydrogen is produced [see Eq. (4)]. As was already shown for similar current densities [$O(10^5$–10^6 A/m^2)], bubble growth occurs mainly by direct diffusion of the hydrogen gas generated at the foot of the bubble due to the high local supersaturation [29]. In addition, smaller bubbles nucleate along the rim of the main bubble and contribute to the bubble growth by coalescence. Only a negligible part of the generated hydrogen diffuses into the bulk electrolyte. Under these circumstances, the amount of hydrogen in the bubble is approximately $n_b \approx n_{\mathrm{H_2}}$; thus the volume of the bubble V can be estimated by inserting Eq. (4) into the ideal gas equation $pV = n_b R_g T$, where R_g is the universal gas constant and p and T are the pressure and temperature inside the bubble. Assuming a circular bubble shape, the bubble diameter can be then calculated by

$$d = \left(\frac{3 R_g T}{p F} \int I(t) dt \right)^{1/3}. \tag{5}$$

Accordingly, the diameter will follow a $d \propto t^{1/3}$ relationship for moderate current changes, which is also in very good agreement with the observations shown in Fig. 2(b). By applying Eq. (5) on each individual growth cycle, the respective detachment diameter can be estimated directly from the measured current.[1] Figure 3 shows the influence of the magnetic induction and electrode potential on the detachment diameter and the corresponding bubble growth time. The latter was determined from the time difference of the respective current peaks [29]. The bubble diameter is considerably reduced

[1]The time instances of the current peaks are used for the integration boundaries of the individual growth cycles. Also note that the contribution of the hydrostatic and Laplace pressure can be neglected [29,30].

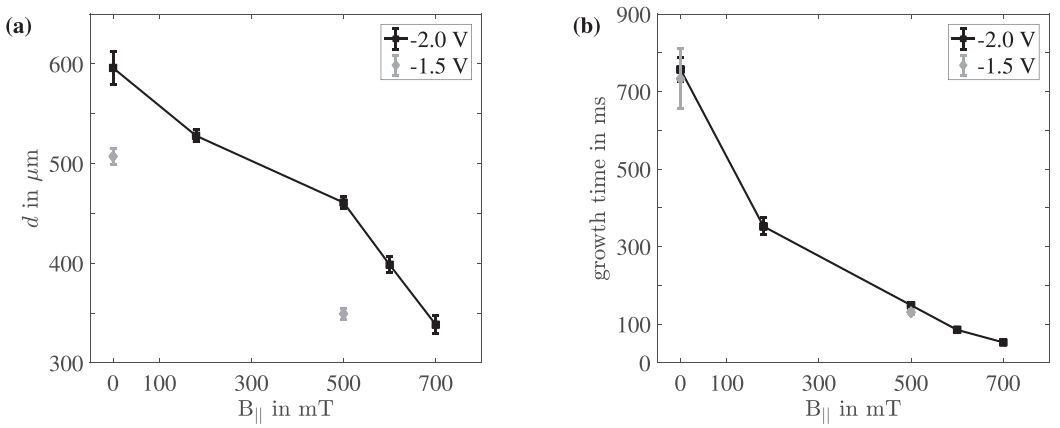

FIG. 3. (a) Bubble detachment diameter and (b) growth time calculated from the measured current signals for different magnetic fields and potentials. The graphs are based on measurements of up to 3000 bubbles. The error bars represent twice the standard deviation ($\pm 2\sigma$).

from about 600 μm at 0 mT to 340 μm at 700 mT. The growth time also decreases significantly from 760 ms to about 50 ms but is nearly not affected by the applied potential. On the other hand, the bubble size becomes larger with the absolute value of the electrode potential, despite the stronger Lorentz forces and the enhanced MHD flow. These results are in very good agreement with previous experiments performed in the same electrochemical setup in an electromagnet with equivalent magnetic flux densities and electrode potentials. Other studies with gas-evolving microelectrodes also report similar effects and indicate a strong influence of the current density [20,30]. For very low current densities and alkaline environments, Zhang and Zeng [12] attributed the increase of the bubble size to an increase of the gas-liquid surface tension at higher electrode potentials. However, electrowetting is also known to improve the wettability of the electrode surface with the applied potential [32]) and, therefore, could also have the opposite effect on the detachment diameter [4].

To gain further insight into the bubble growth and detachment mechanisms, we consider the typical evolution of a single hydrogen bubble at a electrode potential of $E = -2.0$ V and a magnetic induction of $B_{||} = 500$ mT (see Fig. 4). From the beginning of the bubble growth until its detachment, the bubble is slowly sliding away from the center of the microelectrode due to the drag force imposed by the MHD flow [Figs. 4(a) and 4(d)]. The average sliding velocity is $V_{bx} \approx 0.5$ mm/s, approximately half of the average growth velocity $V_{by} \approx 1$ mm/s. The contact angle, calculated from the circular shape fit, is about $18^\circ \pm 5^\circ$ in the beginning of the bubble growth and falls rapidly to zero at approximately 80 ms (not illustrated). From this point onward, the bubble seems to float above the microelectrode and the glass surface, although it is difficult to determine based on the image data if there is no contact at all in the latter case. However, the glass surface is hydrophilic so that a low contact area and contact angle can be generally expected, as also shown by Yang *et al.* [29]. On the other hand, it is clearly visible that the bubble remains connected to the electrode through the carpet of tiny bubbles that are continuously nucleating and coalescing with each other and the main bubble [see, e.g., Fig. 4(b)].[2] Such micron-sized bubbles have been observed to nucleate in less than 0.1 ms at these rather high absolute current densities [29]. The rapid nucleation and coalescence of tiny bubbles is obviously important for the detachment of the main bubble. In order to detach from the nucleation site, the bubble has not only to overcome the surface tension forces acting between

[2]Note that we refer to bubble sliding instead of asymmetric bubble growth as the bubble seems to remain spherical and no conventional neck formation occurs at its foot, where only the coalescence with tiny bubbles is evident.

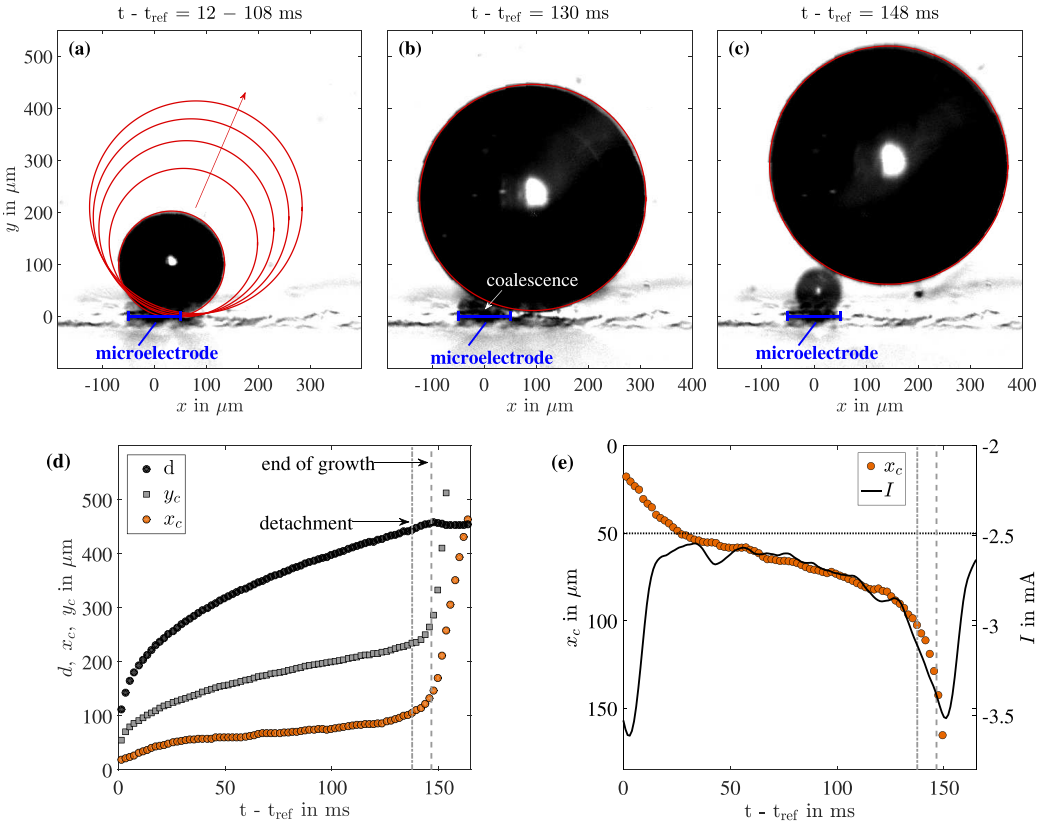

FIG. 4. Growth and detachment of a bubble at $B_{||} = 500$ mT and $E = -2.0\,V$. [(a)–(c)] Series of shadowgraph images superimposed with the circular contour fit in red. In panel (a), several bubble contours with a respective time difference of $\Delta t = 24$ ms have been added. As visualized in panel (b), coalescence of small bubbles with the main bubble is constantly occurring. [(c), (d)] The bubble detachment occurs approximately at t-$t_{\mathrm{ref}} = 137$ ms, after which the bubble continues to grow for a about 10 ms due to coalescence. (d) Evolution of the bubble diameter d and the position of the centroid x_c and y_c; the small decrease of the bubble diameter to the right of the dashed line (end of growth) is the result of the faster bubble motion causing a slightly blurry shadow image. (e) Comparison of bubble position x_c along the electrode and current I.

the bubble and the electrode but also those between the bubble and the coalescing smaller bubbles. A reliable estimation of an effective surface tension force appears almost impossible in view of the complex and highly dynamic coalescence phenomena. These mechanisms might also cause the aforementioned increase of the bubble detachment size with the absolute current density as the nucleation and growth rate of tiny bubbles is enhanced. The implication here is that the effective surface tension force is raised with increasing absolute current density, e.g., due to a larger total contact line length between the main bubble and the coalescing bubbles. The possible increase of the surface tension force is at least evident in the x direction, as can be seen by comparing the sliding trajectories at $B_{||} = 500$ mT for the two different electrode potentials [Fig. 2(b)]. The sliding trajectories are almost identical, although the drag force imposed on the bubble is higher at the potential of $E = -2.0$ V due to the faster MHD flow and larger bubble size, as will be shown later. This could be explained by the counteracting effect of a higher surface tension force.

Before the detachment of the bubble, its centroid is moving with a nearly constant velocity in x and y directions, as can be seen in Fig. 4(d). Detachment occurs approximately at the time instance at which the bubble's centroid, in particular its wall-normal position y_c, clearly begins to accelerate

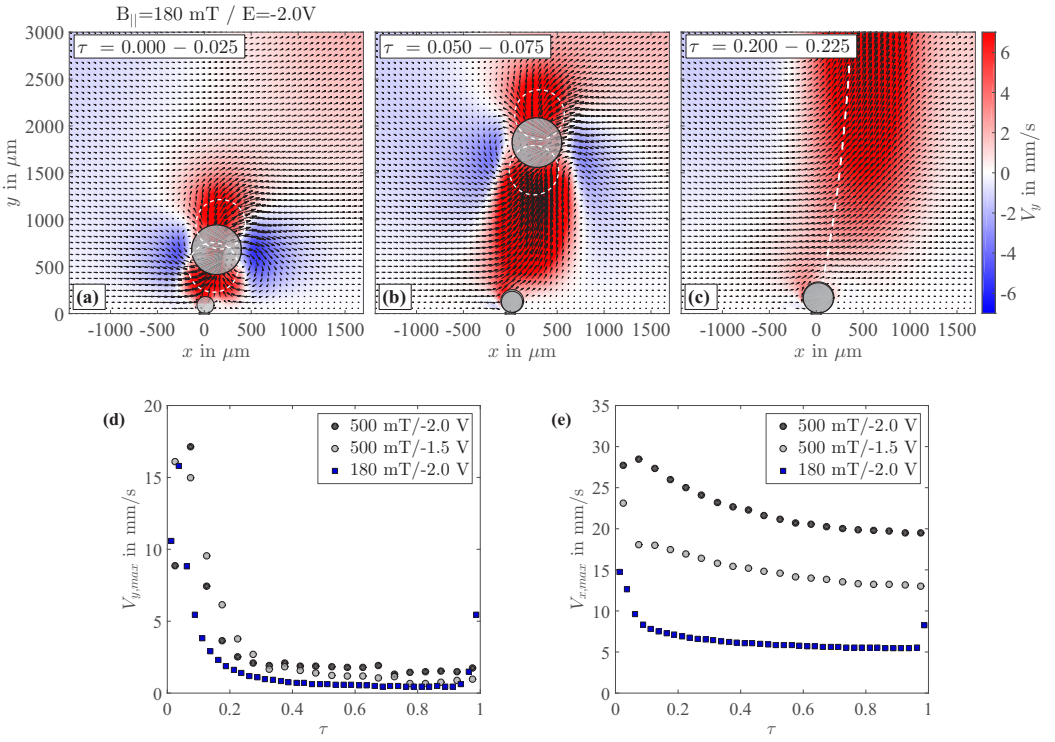

FIG. 5. [(a)–(c)] Phase-averaged velocity fields during the initial growth phases for $B_{||} = 180$ mT and $E = -2.0\ V$. τ is the time normalized by the growth time of the bubble. The contour of the growing bubble is illustrated at the beginning and end of the respective phase. The rising bubble is additionally shown at the center of the phase in panels (a) and (b) while its trajectory is superimposed in panel (c). (d) The maximum wall-normal velocity V_y in a small window of $200 \times 200\ \mu m^2$ on the right side above the growing bubble was used to investigate the influence of the wake on the near-bubble flow. (e) Evolution of the MHD flow characterized by the maximum wall-parallel velocity V_x.

in a continuous manner. After the bubble detaches, it continues to grow for approximately 10 ms [see Fig. 4(d)]. This behavior is also related to the formation of tiny bubbles which quickly coalesce to one bigger bubble on the electrode. Since the newly formed bubble is smaller and thus has a higher Laplace pressure, it is fed into the already rising bubble upon collision. The end of the bubble growth is finally reached when the rising bubble is sufficiently far away from the newly evolving bubble [Fig. 4(c)]. Ultimately, one could argue that the bubble is not completely released until the feeding process is over. However, even though coalescence phenoma are still present, until this point they clearly cannot stop the rise of the detached bubble.

Figure 4(d) compares the evolution of the current with the sliding motion of the bubble. The absolute value of the current decreases at first and begins to increase again as the sliding bubble approaches the edge of the microelectrode ($x_c \approx 50\ \mu$m). The current change from this point on is evidently linked to the motion of the bubble, which increases the available electrode area on its left side while sliding to the right side. As previously mentioned, this is presumable the main cause of the increasing current at higher values of the magnetic induction as the sliding of the bubble is enhanced in a stronger magnetic field [see Fig. 2(b)].

B. The flow field

Figures 5(a)–5(c) show the velocity field during the initial growth phase of the bubble at $B_{||} = 180$ mT. The entrainment by the wake of the previously detached and rising bubble causes

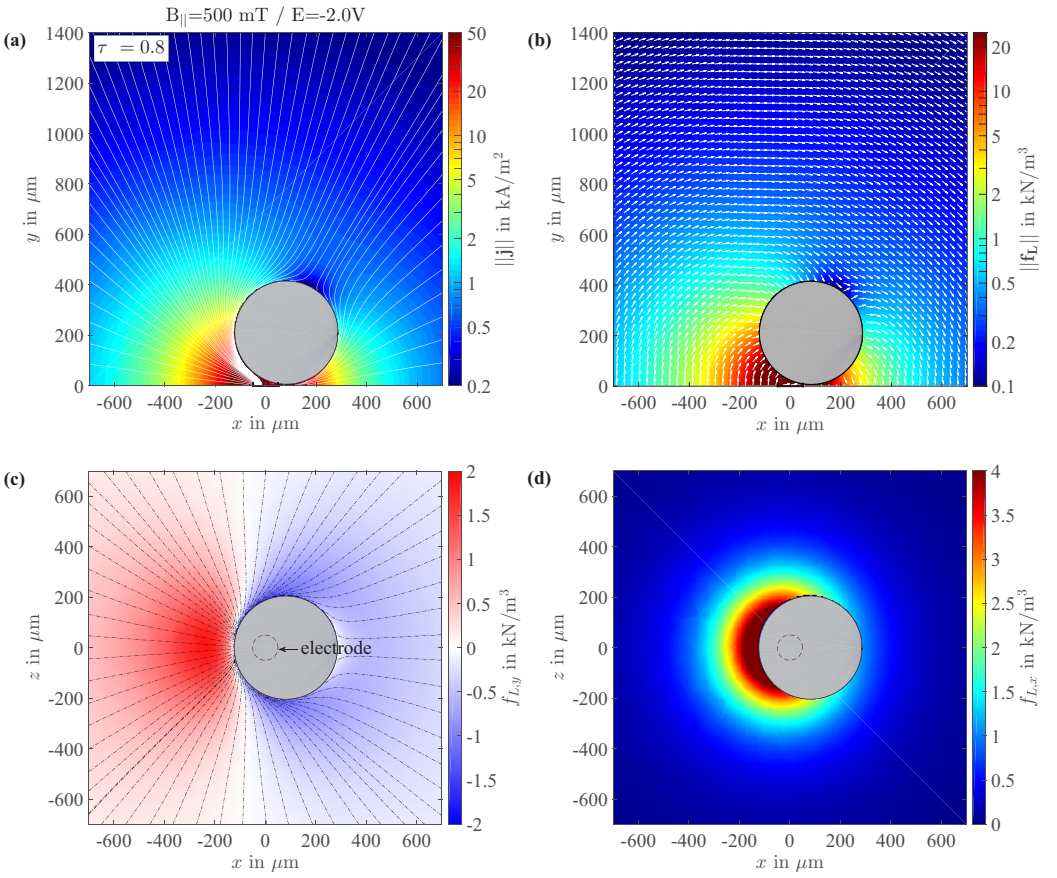

FIG. 6. Numerical results of the current field and the Lorentz force distribution for a late phase of the bubble growth at $B_{||} = 500$ mT and $E = -2.0$ V: (a) Current field lines and density (magnitude scaled logarithmically) in the center plane. (b) Corresponding Lorentz force distribution (magnitude scaled logarithmically, direction indicated by uniform vectors). (c) Wall-normal and (d) wall-parallel component of the Lorentz forces in the horizontal plane passing through the bubble equator. Since the magnetic field is oriented in the z direction, the Lorentz force component in that direction is zero in the entire volume. The dashed line in panel (c) indicate the current field orientation in the horizontal plane.

a significant electrolyte convection close to the bubble, especially in the vertical direction (V_y). However, this effect decays rapidly within the first 20–30% of the bubble growth cycle, as shown in Fig. 5(d) for all investigated cases. The flow is then governed by the much stronger wall-parallel shear flow that is generated by the Lorentz forces [Fig. 5(e)]. Therefore, the wake flow has virtually no effect on the bubble detachment.

As discussed before, the MHD-induced drag force causes the bubble to slowly slide away from the center of the microelectrode to the right. As a result, the access for the electric field to the electrode is restricted on its right side, leading to an asymmetric current field $\mathbf{j}$ and Lorentz force distribution $\mathbf{f_L}$. The generated Lorentz forces $\mathbf{f_L} = \mathbf{j} \times \mathbf{B}$ are generally much higher on the left side of the bubble than on its right side, as becomes evident from the numerical results shown in Fig. 6 for a late phase of the bubble growth [note that the contour values in Figs. 6(a) and 6(b) have been scaled logarithmically]. Since the Lorentz force acts perpendicular to the current and magnetic field ($\mathbf{f_L} = \mathbf{j} \times \mathbf{B}$) and the current field is strongly distorted by the insulating gas bubble, Lorentz force components in x and y directions are generated as illustrated in Fig. 6(b). The wall-normal component $f_{L,y}$ can be of

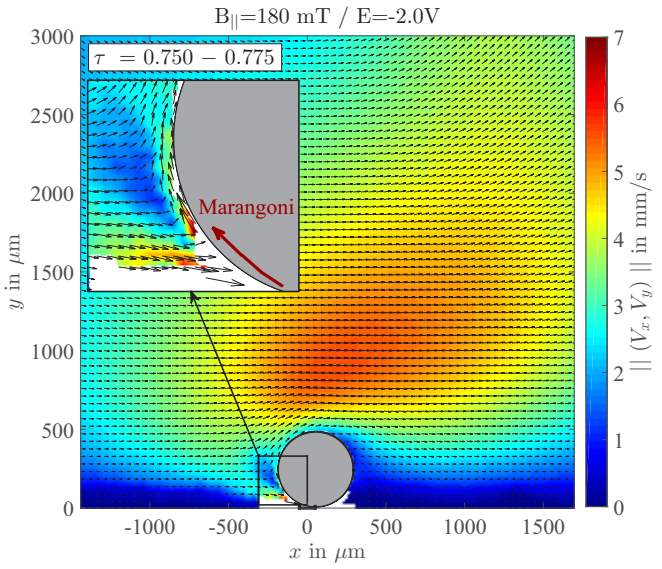

FIG. 7. Phase-averaged velocity field for a late phase of the bubble growth at $B_{||} = 180$ mT and $E = -2.0$ V. The MHD flow is asymmetric as the bubble is pushed away from the microelectrode. Close to the left side of the bubble's foot, a Marangoni flow can be observed [see also Fig. 8(b)].

different sign depending on the orientation of the current field and disappears when the current field orientation is parallel to the magnetic field ($j_x = 0$). This is exemplified in Fig. 6(c), which shows the $f_{L,y}$ distribution in the horizontal plane passing through the equator of the bubble. In contrast, the wall-parallel component $f_{L,x}$ acts only in the positive direction in the entire volume [see Figs. 6(b) and 6(d)].

The characteristic Hartmann number, $\mathrm{Ha} = Bd\sqrt{\sigma_e/\mu_L} \approx 0.04$, is relatively low; hence, viscous forces are strong compared to the induced Lorentz forces and play an important role in the formation of the flow field.[3] The resulting MHD flow is asymmetric as can be seen from the measurements at $B = 180$ mT and $B = 500$ mT shown in Figs. 7 and 8(a), respectively. It is important to note that the formation of the low momentum region on the right side of the bubble is mainly the result of the asymmetric force distribution rather than an inertial flow effect as the Reynolds number of the bubble is small [$O(1 - 10)$]. The high momentum difference between the left and right sides of the bubble increases with the applied magnetic induction and imposes a drag force, which acts against the surface tension forces and causes the bubble to slide to the right. However, it should be mentioned that a smaller drag force can be expected in the case of large electrodes due to a more symmetric Lorentz force distribution.

The velocity distribution around the bubble does not change significantly during its growth and sliding motion, although the maximum fluid velocity above the bubble decreases slightly with time [Fig. 5(e)]. This implies that the local magnitude of the current density becomes lower due to the bubble motion and growth, despite the increase of the absolute electrode current [see Figs. 2 and 4(e)]. The steady numerical simulations performed for a late growth phase of the bubble at $B_{||} = 500$ mT are in very good agreement with the experimental results, as can be seen by comparing Figs. 8(a) and 8(c). Differences occur in a small region near the interface on the left side of the bubble where the numerical results show very low velocities near the stagnation point, in contrast to the experimental data. This can be attributed to the Marangoni convection occurring at the foot of the bubble, which

[3]Electrolyte conductivity $\sigma_e \approx 40$ S/m and dynamic viscosity $\mu_L = 1.2061$ mPas [48].

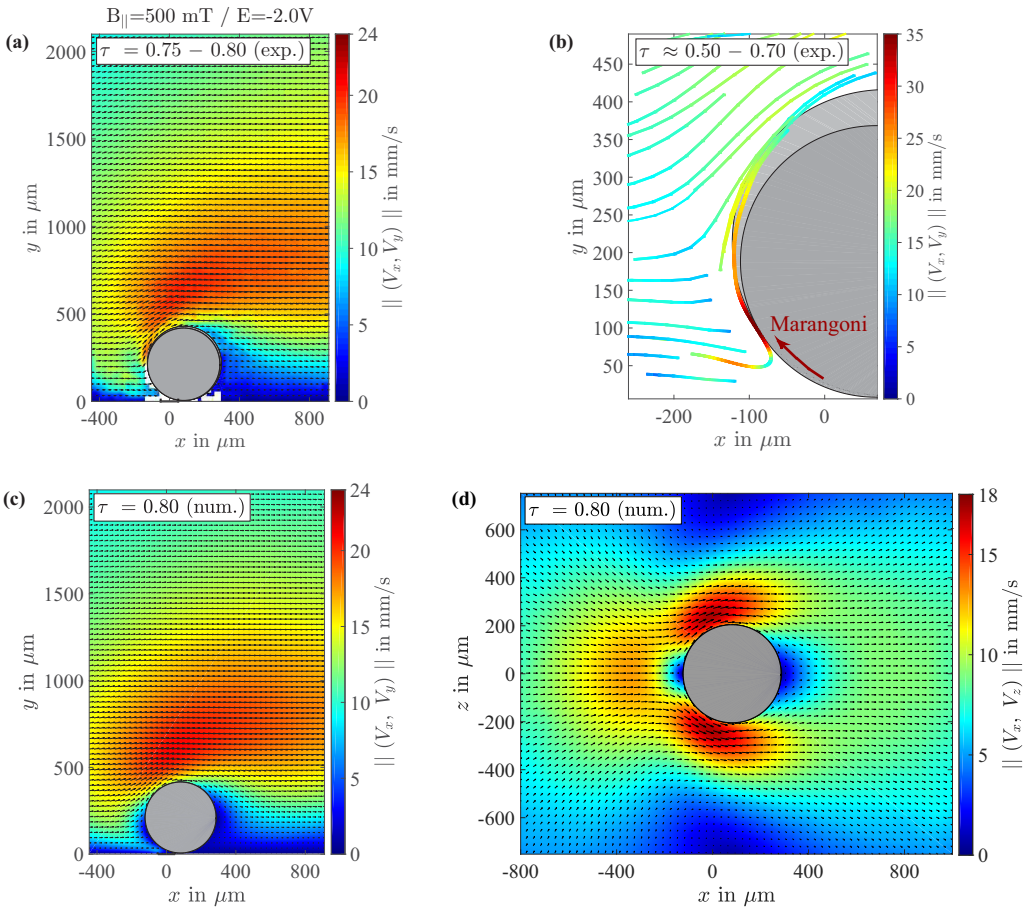

FIG. 8. (a) Phase-averaged velocity field for a late phase of the bubble growth at $B_{||} = 500$ mT and $E = -2.0$ V. (b) Zoom into a few particle trajectories close to the bubble surface, visualizing the Marangoni convection. The bubble contour is shown at the beginning and end of the illustrated phases. Numerical velocity fields in (c) the vertical center plane and (d) the horizontal plane passing through the equator of the bubble.

was not modeled in the numerical approach and will be further discussed below. Figure 8(d) shows the numerical velocity distribution in the horizontal plane passing through the equator of the bubble. As can be seen, the fluid is first accelerated on the left side of the bubble due to the Lorentz forces and then decelerates toward the stagnation point. As expected, the velocities increase again while the fluid is flowing around the bubble. This acceleration is further enhanced by the strong Lorentz forces acting in the region in front of the bubble [see Fig. 6(d)].

As previously mentioned, interfacial flow phenomena occur in addition to the Lorentz-force-driven flow at the foot of the bubble near the electrode, where the concentration of dissolved hydrogen and its gradient are the highest. Now, since dissolved hydrogen can have a substantial surface activity [34], the high local concentration gradients of dissolved hydrogen could give rise to surface tension gradients, which in turn generate shear stresses along the interface, i.e., the solutal Marangoni effect. A thermal Marangoni effect caused by temperature gradients at the interface might also exist as the electrolyte is generally heated close to the electrode due to the high local current density. Although it was theoretically shown by Lubetkin [34] that this effect is generally expected to be several orders of magnitude weaker than the solutal (hydrogen-driven) Marangoni effect, both phenomena should be considered in the case of microelectrodes. The existence of the Marangoni

effect at electrolytically generated hydrogen bubbles is currently investigated in more detail in another study that will be published elsewhere [33]. By measuring the resulting Marangoni flow near the gas-liquid interface for the case without a magnetic field, we were able to show in that study that the magnitude of the generated convection is directly linked to the electric current, i.e., the rate of hydrogen production. An enlarged view of the resulting flow for the $B_{||} = 180$ mT case is shown in Fig. 7. The Marangoni effect causes a jetlike flow along the gas-liquid interface, pointing from the region of low surface tension close to the electrode (high hydrogen concentration and temperature) to the region of higher surface tension further away from the electrode (low hydrogen concentration and temperature). The velocities strongly increase toward the interface as can be seen within a distance of approximately 20 μm from the interface. In addition, the electrolyte accelerates toward the foot of the bubble to replace the fluid in this region. Density gradients in the electrolyte due to concentration gradients of dissolved hydrogen are too small to cause such an intense convection [20,46]. For the case of $B_{||} = 500$ mT illustrated in Fig. 8(a), the high velocity gradients at the interface could not be resolved properly with the current optical magnification. However, the strong fluid acceleration near the interface is exemplified in Fig. 8(b), which shows only a few representative particle trajectories for that case. For neither the $B_{||} = 180$ mT nor the $B_{||} = 500$ mT case can a comparable Marangoni convection be seen on the right side of the bubble, as the current density is low in this region and thus smaller concentration and temperature gradients exist on that side. Obviously, surface tension gradients will also exist along the circumference of the bubble's foot. However, measurements in that plane were not possible with the current experimental setup.

The occurrence of the intense Marangoni convection in electrolysis is important for several reasons. As suggested by Lubetkin [34], the generated shear stresses impose an additional force on the bubble, which in this case acts against its detachment. This force will be later referred to as the Marangoni force and should not be confused with the surface tension force acting between the bubble and the wall. In fact, the gas-liquid surface tension and thus the surface tension force may decrease due to the high concentration of the dissolved hydrogen, which would accelerate the detachment. Further possible effects of the Marangoni convection are the inhibition of bubble coalescence [30,49] and an enhanced mass transfer, which may affect the bubble growth. However, a detailed investigation of the Marangoni convection and its effect will require further simulations and experiments at even higher magnifications.

C. Forces acting on the bubble

The force balance for a bubble growing at a wall can be written as

$$\mathbf{F_B} + \mathbf{F_{CP}} + \mathbf{F_S} + \mathbf{F_{hyd}} + \mathbf{R} = 0, \tag{6}$$

where $\mathbf{F_B}$ is the buoyancy force, $\mathbf{F_{CP}}$ is the contact pressure force, $\mathbf{F_S}$ is the surface tension/capillary force, $\mathbf{F_{hyd}}$ is a group of hydrodynamic forces, and $\mathbf{R}$ is the reaction force acting through the three-phase contact line [25,28]. The inertia of the bubble $\frac{d(m_b \mathbf{V_b})}{dt}$, where m_b is the bubble mass and $\mathbf{V_b}$ is the bubble velocity, was neglected since the bubble mass and its rate of change is very small. The reaction force $\mathbf{R}$ disappears as the bubble detachment is approached. Thus, Eq. (6) with $\mathbf{R} = 0$ is usually considered as the bubble detachment criterion. The respective forces are estimated in the following to assess their influence on the bubble detachment diameter (see, e.g., Refs. [25,28] for a detailed derivation of the forces). The presented estimation is based on the experimental data and numerical simulations performed for $B_{||} = 500$ mT and $E = -2.0$ V at approximately $t - t_{\text{ref}} = 115$ ms, which corresponds to $\tau \approx 0.8$ (see Fig. 4) and represents the situation close to the bubble detachment. The results are summarized in Table I.

The buoyancy force of the bubble is given by

$$\mathbf{F_B} = (\rho_g - \rho_L)\frac{\pi}{6} d^3 \mathbf{g}, \tag{7}$$

TABLE I. Estimation of the forces (given in N) acting on the bubble for $B_{||} = 500$ mT and $E = -2.0$ V at approximately $t - t_{\text{ref}} = 115\ \text{ms}/\tau \approx 0.8$ (see Fig. 4). The MHD-induced forces were obtained from the steady numerical simulations according to Eq. (10). The electrolyte properties at 20 °C were set to $\rho_L = 1060\ \text{kg/m}^3$, $\mu_L = 1.2061$ mPas, and $\sigma = 73$ mN/m [48].

Term	x component (N)	y component (N)
F_B		$+3.9 \times 10^{-7}$
F_{CP}		$O(+10^{-7})$ for 14 μm $< d_c <$ 44 μm
F_S	$\sim F_{p,x} + F_{v,x}$	N/A
F_{Growth}		-7×10^{-9}
F_p	$+6.48 \times 10^{-8}$	$+7.37 \times 10^{-8}$
F_v	$+6.13 \times 10^{-8}$	$+4.65 \times 10^{-9}$
$F_p + F_v$	$+1.26 \times 10^{-7}$	$+7.83 \times 10^{-8}$
$F_{\text{Marangoni}}$	N/A	N/A

where ρ_G, ρ_L, and $\mathbf{g}$ are the density of the gaseous phase (hydrogen), the density of the liquid phase, and the gravitational field, respectively. The contact pressure force $\mathbf{F_{CP}}$

$$\mathbf{F_{CP}} = \int_{S_f} (p_c - p_G)\mathbf{n} dS \approx \pi \frac{d_c^2}{4} \frac{2\sigma}{d/2} \tag{8}$$

is acting in the same direction as the buoyancy and is caused by the overpressure inside the bubble (Laplace pressure) and the fact that the bubble is not surrounded by the liquid below its foot. S_f, p_c, p_G, d_c, and σ in Eq. (8) are the surface of the bubble foot, the reference pressure of the liquid at the contact point with the wall, the pressure inside the bubble, the contact diameter, and the surface tension between the gas and the liquid, respectively. Depending on the size of the bubble and the contact diameter, the contact pressure force can be of the same order or even larger than the buoyancy (see Table I), but usually becomes small when the bubble detachment is approached [25]. However, since the contact area cannot be obtained from the experimental data due to the highly dynamic coalescence phenomena at the foot of the bubble, a reliable estimate of the contact pressure force is currently not possible if at all applicable for this particular situation. The surface tension force is given by

$$\mathbf{F_S} = \int_0^{2\pi} \frac{d_c}{2} \sigma \mathbf{t}(\phi) d\phi, \tag{9}$$

where $\mathbf{t}$ is the vector tangential to the gas-liquid interface and perpendicular to the contact line and ϕ is the polar angle along the the contact line. The surface tension force is the main force that keeps the bubble attached to the wall and impedes the bubble sliding in the case of an asymmetric contact angle distribution. Similar to the contact pressure force, a reliable estimate cannot be obtained from the experimental data considering the complex coalescence phenomena discussed previously. The hydrodynamic forces acting on the bubble can be written as the sum of the pressure force $\mathbf{F_p}$ and the viscous force $\mathbf{F}_v$

$$\mathbf{F_{hyd}} = \mathbf{F_p} + \mathbf{F}_v = -\int_{S_b} (p_L - p_c)\mathbf{n}\, dS \ + \int_{S_b} \tau_L \cdot \mathbf{n}\, dS, \tag{10}$$

where S_b is the bubble surface exposed to the liquid, p_L is the hydrodynamic pressure in the liquid, and $\tau_{\mathbf{L}}$ is the stress tensor due to viscous normal stresses and shear stresses. The previously discussed Marangoni effect causes shear stresses at the interface and thus directly contributes to the viscous force. However, its contribution cannot be estimated from the numerical simulations as this effect was not modeled.

The hydrodynamic forces are usually separated into quasisteady and unsteady forces. The quasisteady parts, which to a large extent are a result of the MHD flow, can be obtained from the steady numerical simulations using Eq. (10), while its unsteady contribution is disregarded due to the relatively small velocity change with time during the last stages of the bubble growth [Fig. 5(e)]. Moreover, the drag term due to bubble sliding was not considered as the sliding velocity is very low compared to the wall-parallel flow velocity. On the other hand, to estimate the wall-normal quasisteady drag force due to the bubble growth, we may use the expression derived by Magnaudet *et al.* [50] for a bubble moving in a linear shear flow in the vicinity of a horizontal wall at low Reynolds numbers (Re $\ll 1$). This expression includes the Stokes drag for a clean inviscid bubble and a correction to account for the vicinity to the wall:

$$\mathrm{F}_{\mathrm{Growth,y}} = -4\pi\mu_L \frac{d}{2} V_{by} k_c, \quad k_c = \left\{1 - \frac{3}{4}\frac{d}{2y_c} - \frac{9}{64}\left(\frac{d}{2y_c}\right)^4 + \mathcal{O}\left[\left(\frac{d}{2y_c}\right)^5\right]\right\}^{-1}. \tag{11}$$

Here, μ_L and V_{by} denote the dynamic viscosity of the fluid and bubble growth velocity, respectively. Since Eq. (11) is only valid for $d/(2y_c) < 0.7$ and overestimates the drag force beyond this limit [50], we use a linear extrapolation of the correction factor k_c, similar to the approach of Duhar and Colin [28]. For a bubble touching the wall [$d/(2y_c) = 1$], this yields $k_c = 3.65$ (while $k_c = 1$ is approached far away from the wall). Furthermore, the unsteady hydrodynamic forces, i.e., the added-mass force and history force [51], can be considered to be small during the bubble growth at the present growth rates. Using the expression from Thorncroft *et al.* [25], it can be shown that the added-mass force is $O(10^{-10}$ N), which is three orders of magnitude lower than the buoyancy force.

In Table I, the contributions of the different forces are listed. The MHD-induced pressure and viscous contribution to the drag (x direction) are of the same order, which can be generally expected in a low Reynolds number flow [52,53]. As for the MHD-induced lift force (y direction), the largest contribution comes from the pressure part, while the viscous part adds comparatively little. Note that the total MHD lift force (7.8×10^{-8} N) amounts to approximately 62% of the imposed drag (1.3×10^{-7} N), which is relatively large and rather unusual. This can be explained by the strong Lorentz forces acting near the foot of the bubble, particularly on its left side [Fig. 6(b)], where the flow slows down in the region close to the stagnation point and has only limited space to pass the bubble due to the vicinity of the wall.

Comparing the resulting forces in wall-normal (y) direction, it can be seen that the force balance before the detachment of the bubble is mainly influenced by the buoyancy, contact pressure, MHD lift, and surface tension forces. The MHD lift force is approximately 20% of the buoyancy; hence, it certainly contributes to the accelerated bubble detachment. The wall-normal drag due to the bubble growth, on the other hand, is relatively small at these growth rates and not likely to cause the significant increase of the detachment diameter with the applied current density or respective electrode potential. The most plausible explanation of this effect is a change of the effective surface tension force, presumably linked to the enhanced formation and coalescence of tiny bubbles at the foot of the main bubble. The force related to the Marangoni effect $F_{\mathrm{Marangoni}}$ might also contribute to this behavior. Its contribution to the force balance and its influence on the hydrodynamics should be addressed in future studies. In addition to the MHD-induced lift force, the corresponding drag seems to play a major role for the bubble departure, causing the bubble to slide away from the microelectrode, which in turn might also reduce the surface tension forces F_{Sy} acting between the bubble and the coalescing bubbles or the wall.

IV. CONCLUSIONS

The growth and detachment of single hydrogen gas bubbles formed at a Pt microelectrode in the presence of a MHD shear flow were experimentally and numerically studied. For all investigated cases, the bubble is pushed to the side due to strong drag force imposed by the MHD flow. As a result, the active electrode area and the resulting current and growth rate are increased. Moreover,

the bubble diameter can be significantly reduced with increasing magnetic induction, which is essential to improve the performance of water electrolysis. The force analysis has shown that both the MHD-induced drag and lift force contribute to this effect. However, since the drag force displaces the bubble on the microelectrode, an asymmetric Lorentz force distribution is generated. This asymmetry might cause a higher drag and lift force as opposed to the case of larger electrodes in real electrolyzers, where a more symmetric Lorentz force distribution can be expected. The results further indicate that at these high current densities, the coalescence of tiny bubbles formed at the foot of the main bubble might influence the effective surface tension force that keeps the bubble attached to the electrode. By comparison, the contribution of the the wall-normal drag due to the bubble growth was found to be relatively small and is not expected to influence the detachment diameter significantly. Finally, the flow measurements close to the bubble foot show that considerable Marangoni effects occur presumably due to high concentration gradients of dissolved hydrogen and temperature gradients at the gas-liquid interface, which gives rise to surface tension gradients. The Marangoni convection is not only relevant for the mass transfer but might also impose an additional force that retards the detachment of the bubble [34]. However, additional investigations and measurements at even higher magnifications are necessary to further characterize these phenomena.

ACKNOWLEDGMENTS

The financial support from DFG (German Research Foundation) through the Emmy-Noether Research Group program under Grant No. CI 185/3 (D.B. and C.C.) and the projects TS 311/2 (F.K. and M.U.) and EC 201/4 (X.Y. and K.E.) is gratefully acknowledged.

[1] H. Vogt, On the supersaturation of gas in the concentration boundary layer of gas evolving electrodes, Electrochim. Acta **25**, 527 (1980).
[2] C. Sillen, The effect of gas bubble evolution on the energy efficiency in water electrolysis, Ph.D. thesis, Eindhoven University of Technology, Eindhoven, Netherlands, 1983.
[3] P. J. Sides, Phenomena and effects of electrolytic gas evolution, in *Modern Aspects of Electrochemistry* (Plenum Press, New York, 1986), Vol. 18, pp. 303–354.
[4] H. Vogt and R. J. Balzer, The bubble coverage of gas-evolving electrodes in stagnant electrolytes, Electrochim. Acta **50**, 2073 (2005).
[5] K. Zeng and D. Zhang, Recent progress in alkaline water electrolysis for hydrogen production and applications, Prog. Energy Combust. Sci. **36**, 307 (2010).
[6] M. Wang, Z. Wang, X. Gong, and Z. Guo, The intensification technologies to water electrolysis for hydrogen production: A review, Renew. Sustain. Energy Rev. **29**, 573 (2014).
[7] F. Hine and K. Murakami, Bubble effects on the solution IR drop in a vertical electrolyzer under free and forced convection, J. Electrochem. Soc. **127**, 292 (1980).
[8] F. Hine, M. Yasuda, R. Nakamura, and T. Noda, Hydrodynamic studies of bubble effects on the ir-drops in a vertical rectangular cell, J. Electrochem. Soc. **122**, 1185 (1975).
[9] B. E. Bongenaar-Schlenter, L. J. J. Janssen, S. J. D. van Stralen, and E. Barendrecht, The effect of the gas void distribution on the ohmic resistance during water electrolytes, J. Appl. Electrochem. **15**, 537 (1985).
[10] J. Eigeldinger and H. Vogt, The bubble coverage of gas-evolving electrodes in a flowing electrolyte, Electrochim. Acta **45**, 4449 (2000).
[11] B. J. Balzer and H. Vogt, Effect of electrolyte flow on the bubble coverage of vertical gas-evolving electrodes, J. Electrochem. Soc. **150**, E11 (2003).
[12] D. Zhang and K. Zeng, Evaluating the behavior of electrolytic gas bubbles and their effect on the cell voltage in alkaline water electrolysis, Ind. Eng. Chem. Res. **51**, 13825 (2012).
[13] L. M. A. Monzon and J. M. D. Coey, Magnetic fields in electrochemistry: The Lorentz force: A mini-review, Electrochem. Commun. **42**, 38 (2014).

[14] J. A. Koza, S. Mühlenhoff, P. Żabiński, P. Nikrityuk, K. Eckert, M. Uhlemann, A. Gebert, T. Weier, L. Schultz, and S. Odenbach, Hydrogen evolution under the influence of a magnetic field, Electrochim. Acta **56**, 2665 (2011).
[15] T. Iida, H. Matsushima, and Y. Fukunaka, Water electrolysis under a magnetic field, J. Electrochem. Soc. **154**, E112 (2007).
[16] Z. Diao, P. A. Dunne, G. Zangari, and J. M. D. Coey, Electrochemical noise analysis of the effects of a magnetic field on cathodic hydrogen evolution, Electrochem. Commun. **11**, 740 (2009).
[17] H. Matsushima, T. Iida, and Y. Fukunaka, Observation of bubble layer formed on hydrogen and oxygen gas-evolving electrode in a magnetic field, J. Solid State Electrochem. **16**, 617 (2012).
[18] H. Matsushima, T. Iida, and Y. Fukunaka, Gas bubble evolution on transparent electrode during water electrolysis in a magnetic field, Electrochim. Acta **100**, 261 (2013).
[19] T. Weier, D. Baczyzmalski, J. Massing, S. Landgraf, and C. Cierpka, The effect of a Lorentz-force-driven rotating flow on the detachment of gas bubbles from the electrode surface, Int. J. Hydrogen Energy **42**, 20923 (2017).
[20] D. Baczyzmalski, F. Karnbach, X. Yang, G. Mutschke, M. Uhlemann, K. Eckert, and C. Cierpka, On the electrolyte convection around a hydrogen bubble evolving at a microelectrode under the influence of a magnetic field, J. Electrochem. Soc. **163**, E248 (2016).
[21] T. Weier and S. Landgraf, The two-phase flow at gas-evolving electrodes: Bubble-driven and Lorentz-force-driven convection, Eur. Phys. J.: Spec. Top. **220**, 313 (2013).
[22] D. Baczyzmalski, T. Weier, C. J. Kähler, and C. Cierpka, Near-wall measurements of the bubble- and Lorentz-force-driven convection at gas-evolving electrodes, Exp. Fluids **56**, 162 (2015).
[23] J. F. Klausner, R. Mei, D. M. Bernhard, and L. Z. Zeng, Vapor bubble departure in forced convection boiling, Int. J. Heat Mass Transfer **36**, 651 (1993).
[24] L. Z. Zeng, J. F. Klausner, D. M. Bernhard, and R. Mei, A unified model for the prediction of bubble detachment diameters in boiling systems, II: Flow boiling, Int. J. Heat Mass Transfer **36**, 2271 (1993).
[25] G. E. Thorncroft, J. F. Klausner, and R. Mei, Bubble forces and detachment models, Multiphase Sci. Technol. **13**, 42 (2001).
[26] R. Situ, T. Hibiki, M. Ishii, and M. Mori, Bubble lift-off size in forced convective subcooled boiling flow, Int. J. Heat Mass Transfer **48**, 5536 (2005).
[27] D. Chen, L. Pan, and S. Ren, Prediction of bubble detachment diameter in flow boiling based on force analysis, Nucl. Eng. Des. **243**, 263 (2012).
[28] G. Duhar and C. Colin, Dynamics of bubble growth and detachment in a viscous shear flow, Phys. Fluids **18**, 077101 (2006).
[29] X. Yang, F. Karnbach, M. Uhlemann, S. Odenbach, and K. Eckert, Dynamics of single hydrogen bubbles at a platinum microelectrode, Langmuir **31**, 8184 (2015).
[30] D. Fernández, P. Maurer, M. Martine, J. M. D. Coey, and M. E. Möbius, Bubble formation at a gas-evolving microelectrode, Langmuir **30**, 13065 (2014).
[31] G. Sakuma, Y. Fukunaka and H. Matsushima, Nucleation and growth of electrolytic gas bubbles under microgravity, Int. J. Hydrogen Energy **39**, 7638 (2014).
[32] F. Mugele and J. C. Baret, Electrowetting: From basics to applications, J. Phys.: Cond. Matter **17**, R705 (2005).
[33] X. Yang, D. Baczyzmalski, C. Cierpka, and K. Eckert, Marangoni convection at electrogenerated hydrogen microbubbles (unpublished).
[34] S. Lubetkin, The motion of electrolytic gas bubbles near electrodes, Electrochim. Acta **48**, 357 (2002).
[35] P. Boissonneau and P. Byrne, An experimental investigation of bubble-induced free convection in a small electrochemical cell, J. Appl. Electrochem. **30**, 767 (2000).
[36] F. Karnbach, X. Yang, G. Mutschke, J. Fröhlich, J. Eckert, A. Gebert, K. Tschulik, K. Eckert, and M. Uhlemann, Interplay of the open circuit potential-relaxation and the dissolution behavior of a single H_2 bubble generated at a Pt microelectrode, J. Phys. Chem. C **120**, 15137 (2016).
[37] H. Liu, L. Pan, and J. Wen, Numerical simulation of hydrogen bubble growth at an electrode surface, Can. J. Chem. Eng. **94**, 192 (2016).

[38] H. Liu, L. Pan, H. Huang, Q. Qin, P. Li, and J. Wen, Hydrogen bubble growth at micro-electrode under magnetic field, J. Electroanal. Chem. **754**, 22 (2015).
[39] Q. Chen, L. Luo, H. Faraji, S. W. Feldberg, and H. S. White, Electrochemical measurements of single H_2 nanobubble nucleation and stability at pt nanoelectrodes, J. Phys. Chem. Lett. **5**, 3539 (2014).
[40] D. Fernández, M. Martine, A. Meagher, M. E. Möbius, and J. M. D. Coey, Stabilizing effect of a magnetic field on a gas bubble produced at a microelectrode, Electrochem. Comm. **18**, 28 (2012).
[41] L. Luo and H. S. White, Electrogeneration of single nanobubbles at sub-50-nm-radius platinum nanodisk electrodes, Langmuir **29**, 11169 (2013).
[42] M. Rossi, R. Segura, C. Cierpka, and C. J. Kähler, On the effect of particle image intensity and image preprocessing on depth of correlation in micro-PIV, Exp. Fluids **52**, 1063 (2012).
[43] C. Cierpka and C. J. Kähler, Particle imaging techniques for volumetric three-component (3D3C) velocity measurements in microfluidics, J. Vis. **15**, 1 (2012).
[44] C. J. Kähler, S. Scharnowski, and C. Cierpka, On the uncertainty of digital PIV and PTV near walls, Exper. Fluids **52**, 1641 (2012).
[45] C. Cierpka, R. Segura, R. Hain, and C. J. Kähler, A simple single camera 3C3D velocity measurement technique without errors due to depth of correlation and spatial averaging for microfluidics, Meas. Sci. Technol. **21**, 045401 (2010).
[46] G. Mutschke, D. Baczyzmalski, C. Cierpka, F. Karnbach, M. Uhlemann, X. Yang, K. Eckert, and J. Fröhlich, Numerical simulation of mass transfer and convection near a hydrogen bubble during water electrolysis in a magnetic field, Magnetohydrodyn. **53**, 193 (2017).
[47] C. A. C. Sequeira, D. M. F. Santos, B. Šljukić, and L. Amaral, Physics of electrolytic gas evolution, Brazil. J. Phys. **43**, 199 (2013).
[48] D. R. Lide, *CRC Handbook of Chemistry and Physics*, 87th ed. (CRC Press, Boca Raton, FL, 2006).
[49] P. K. Weissenborn and R. J. Pugh, Surface tension of aqueous solutions of electrolytes: Relationship with ion hydration, oxygen solubility, and bubble coalescence, J. Colloid Interface Sci. **184**, 550 (1996).
[50] J. Magnaudet, S. H. U. Takagi, and D. Legendre, Drag, deformation, and lateral migration of a buoyant drop moving near a wall, J. Fluid Mech. **476**, 115 (2003).
[51] J. Magnaudet, Small inertial effects on a spherical bubble, drop, or particle moving near a wall in a time-dependent linear flow, J. Fluid Mech. **485**, 115 (2003).
[52] D. Legendre and J. Magnaudet, The lift force on a spherical bubble in a viscous linear shear flow, J. Fluid Mech. **368**, 81 (1998).
[53] R. Clift, J. R. Grace, and M. E. Weber, *Bubbles, Drops, and Particles* (Academic Press, San Diego, CA, 1978).